The Astrophysical Journal, 652:650–660, 2006 November 20

FIRST SURFACE-RESOLVED RESULTS WITH THE INFRARED OPTICAL TELESCOPE ARRAY IMAGING INTERFEROMETER: DETECTION OF ASYMMETRIES IN ASYMPTOTIC GIANT BRANCH STARS

S. Ragland,[1,2] W. A. Traub,[1,3] J.-P. Berger,[4] W. C. Danchi,[5] J. D. Monnier,[6] L. A. Willson,[7] N. P. Carleton,[1] M. G. Lacasse,[1] R. Millan-Gabet,[8] E. Pedretti,[6] F. P. Schloerb,[9] W. D. Cotton,[10] C. H. Townes,[11] M. Brewer,[9] P. Haguenauer,[12] P. Kern,[4] P. Labeye,[13] F. Malbet,[4] D. Malin,[9] M. Pearlman,[1] K. Perraut,[9] K. Souccar,[9] and G. Wallace[9]

Received 2004 June 28; accepted 2006 June 20

ABSTRACT

We have measured nonzero closure phases for about 29% of our sample of 56 nearby asymptotic giant branch (AGB) stars, using the three-telescope Infrared Optical Telescope Array (IOTA) interferometer at near-infrared wavelengths (*H* band) and with angular resolutions in the range 5–10 mas. These nonzero closure phases can only be generated by asymmetric brightness distributions of the target stars or their surroundings. We discuss how these results were obtained and how they might be interpreted in terms of structures on or near the target stars. We also report measured angular sizes and hypothesize that most Mira stars would show detectable asymmetry if observed with adequate angular resolution.

Subject headings: circumstellar matter — stars: AGB and post-AGB — stars: imaging — stars: spots — surveys — techniques: interferometric

Online material: color figure

1. INTRODUCTION

The stars in this study are all asymptotic giant branch (AGB) stars, that is, stars found at or near the tip of the AGB in the H-R diagram. They are low- to intermediate-mass stars, having already spent most of their lives as normal stars, and currently heading toward their deaths probably in the form of planetary nebulae (PNe), leaving the central star as a white dwarf. Most AGB stars are variable in brightness; those with relatively regular and large-amplitude visual variations (>2.5 mag) with periods in the range 100–1000 days are classified as Mira variables. The Mira variables and some of the other, semiregular (SR) or irregular (Irr) variables have observed mass-loss rates ranging from 10^{-7} to $>10^{-5}$ $M_{\odot}$ yr^{-1} (Knapp & Morris 1985). Diameter changes, opacity changes, and possibly other processes such as convection contribute to the brightness variation in these stars.

The Mira stage of evolution has been identified as marking the onset of the "superwind" phase, i.e., that evolutionary stage in which mass-loss rates rapidly increase and result in the termination of AGB evolution (Bowen & Willson 1991; Willson 2000). These stars thus serve as markers for the tip of the AGB in various populations, something already known for the shorter period cases from the few Mira variables that appear in globular clusters such as 47 Tuc (Frogel et al. 1981).

Mira variables with close companion white dwarfs usually are classified as symbiotic systems (Allen 1984; Whitelock 1987; Luthardt 1992; Belczyński et al. 2000). A few Mira variables are known to have companions but are not (or are only very mildly) symbiotic systems; this includes *o* Cet (=Mira), with a probable white dwarf companion in a multicentury orbit (Reimers & Cassatella 1985; Wood & Karovska 2004). Statistics for the binarity of Mira variables are otherwise quite uncertain, in part because the expected orbital velocity amplitudes for a close companion, 30 km s^{-1} at 1 AU and 10 km s^{-1} around 5 AU, are very similar to the shock amplitudes of 20–30 km s^{-1} produced by the Mira pulsation itself (Hinkle et al. 1984).

In this paper we use the word "asymmetry" to mean that part of the two-dimensional brightness distribution that cannot be made symmetric with respect to a reflection through a point. Thus, for example, an elliptical uniform disk or an equal-brightness binary system are both symmetric, but a binary with unequal brightness or a star with an off-centered bright/dark spot is asymmetric.

Departure from circular symmetry has been known in AGB stars from various high angular resolution observations (Karovska et al. 1991, 1997; Wilson et al. 1992; Haniff et al. 1992; Richichi et al. 1995; Ragland 1996; Weigelt et al. 1996; Lattanzi et al. 1997; Wittkowski et al. 1998; Tuthill et al. 1997, 1999, 2000; Hofmann et al. 2000; Thompson et al. 2002; Monnier et al. 2004a; Weiner et al. 2006). The observed departures from circular symmetry have been interpreted in terms of either elliptical distortions or an otherwise symmetric photosphere containing

[1] Harvard-Smithsonian Center for Astrophysics, 60 Garden Street, Cambridge, MA 02138.
[2] Currently at California Association for Research in Astronomy, 65-1120 Mamalahoa Highway, Kamuela, HI 96743; sragland@keck.hawaii.edu.
[3] Jet Propulsion Laboratory, M/S 301-451, 4800 Oak Grove Drive, Pasadena CA, 91109.
[4] Laboratoire d'Astrophysique de Grenoble, 414 Rue de la Piscine, F-38400 Saint Martin d'Heres, France.
[5] NASA Goddard Space Flight Center, Exoplanets and Stellar Astrophysics, Code 667, Greenbelt, MD 20771.
[6] University of Michigan at Ann Arbor, Department of Astronomy, 500 Church Street, Ann Arbor, MI 48109-1090.
[7] Department of Physics and Astronomy, Iowa State University, Ames, IA 50014.
[8] Michelson Science Center, California Institute of Technology, Pasadena, 770 S. Wilson Avenue, Pasadena, CA 91125.
[9] University of Massachusetts at Amherst, Department of Astronomy, LGRT-B 619E, 710 North Pleasant Street, Amherst, MA 01003-9305.
[10] National Radio Astronomy Observatory, 520 Edgemont Road, Charlottesville, VA 22903.
[11] University of California at Berkeley, Space Science Laboratory, Berkeley, CA 94725-7450.
[12] ALCATEL Space Industries, 100 boulevard du Midi, BP99, 06322 Cannes, France.
[13] LETI, CEA-Grenoble, 17 rue des Martyrs, 38 054 Grenoble CEDEX 9, France.

localized compact features. However, no consensus exists as to the mechanism that would cause such departures from apparent circular symmetry.

Dust shells surrounding AGB stars have observed asymmetries as well, such as in Mira (Lopez et al. 1997) and the carbon stars IRC +10216 (CW Leo; Tuthill et al. 2000), CIT 6 (Monnier et al. 2000), and IK Tau (Weiner et al. 2006), among others. The connection between apparent surface features and the morphology of the dust shells has not been established.

About 50% of all PNe display bipolar symmetry (Zuckerman & Aller 1986), but only a small fraction of circumstellar envelopes show bipolarity. A surprisingly large number of proto-PNe show roughly circular arcs surrounding a bipolar core, suggesting that in most cases the AGB mass loss is spherically symmetric and the asymmetry seen in the PN occurs well after the Mira stage (Su 2004; Willson & Kim 2004). Recent studies of jets around a few AGB stars (Kellogg et al. 2001; Imai et al. 2002; Sahai et al. 2003; Sokoloski & Kenyon 2003; Brocksopp et al. 2004) from radio, X-ray, or *Hubble Space Telescope* (*HST*) observations suggest that those stars showing substantial asymmetry may all have a low-mass stellar companion accreting mass from the AGB primary. Recent SiO maser observations of AGB stars show departures from spherical symmetry (Diamond et al. 1994; Greenhill et al. 1995; Diamond & Kemball 2003; Cotton et al. 2004; Soria-Ruiz et al. 2004). The observed circumstellar SiO masers tend to occur in clumpy, partial rings centered on the central star (Diamond et al. 1994). Cotton et al. (2004) observed nine stars in SiO, at least two of them known binaries, and used the modeling of Humphreys et al. (2002) in discussing the results. SiO maser emission comes from $\sim$2 AU or $\sim 2R_*$ where the outflow velocity gradient along the line of sight is small. The special conditions required for maser emission potentially give rise to bias in the statistics of asymmetry in the sample population of stars.

In this paper we report the initial results from one phase of a larger program, the Mira Imaging Project, to investigate asymmetries in AGB stars using three interferometer facilities, each capable of making closure-phase measurements. These facilities are the Infrared Optical Telescope Array (IOTA), the Infrared Spatial Interferometer (ISI), and the Very Long Baseline Array (VLBA). This paper focuses on IOTA results.

Subsequent to the work reported here, and as a part of the ongoing Mira Imaging Project, selected Mira targets with positive closure-phase signal from our survey have been revisited at different pulsational phases, baselines, position angles, and wavelengths in order to characterize the observed asymmetry. The results of this ongoing study will be presented elsewhere. In this paper, we present the initial survey results for all our targets.

2. OBSERVATIONS

The observations reported here were carried out during the commissioning phase of the IOTA three-telescope array (Traub et al. 2004) and integrated-optics beam-combiner, IONIC (Berger et al. 2003), operating in the H-band (1.65 μm) atmospheric window. Observations of binary stars taken with the same instrumental configurations were reported by Monnier et al. (2004b) and Kraus & Schloerb (2004). We report here the results of the first phase of our program in which we have studied 56 evolved giants (Tables 1 and 2) including 35 Mira stars, 18 SR variables, and 3 Irr variables[14] looking for asymmetry in their brightness profiles.

[14] δ2 Lyr is classified in the CGCVS (Samus et al. 2004) with an uncertainty as a SR variable, and no period estimate is available in the literature. We consider this target to be an Irr variable for the purpose of this paper.

We report observations taken during six observing runs during 2002 May to 2003 May. Observations were taken either with a standard H-band filter ($\lambda = 1.65$ μm, $\Delta\lambda = 0.3$ μm) or with a narrowband filter ($\lambda = 1.64$ μm, $\Delta\lambda = 0.1$ μm). Typically, 5 minutes of program star observations were followed by nearby calibrator observations under identical instrumental configurations. For the observations taken during 2003 March and May observing runs, we used ND filters for the bright targets, since we had excellent optical throughput with newly coated primary mirrors and well-optimized beam train. On each star, we record four sets of data files, each containing about 500 scans. A scan consists of changing the optical path difference between two beams by roughly 75 μm in sawtooth form. We then take about 400 scans of shutter data for calibration. The shutter data sequence consists of allowing only one beam at a time (telescope A, B, and then C) and at the end blocking all three beams. Each scan takes about 100 ms.

All targets were observed with a three-baseline interferometer configuration, forming a closed triangle. Earth rotation enables closure-phase measurements at slightly different projected baselines (and hence different closed triangles) when observations are made at different hour angles. We have adopted baseline bootstrapping (Mozurkewich & Armstrong 1992) at the IOTA whereby fringes are tracked on two short baselines, while science data are recorded on all three baselines simultaneously, enabling low-visibility measurements on the third (long) baseline. Details of the detector camera and the fringe tracker algorithm used for this work are reported by Pedretti et al. (2004) and Pedretti et al. (2005), respectively.

IOTA's maximum baseline of $B = 38$ m yields an angular resolution of $\lambda/2B \simeq 4$ mas at 1.65 μm. The present faint limit with the IONIC beam-combiner is $H \simeq 7$ for the broadband filter and $H \simeq 5$ for the three narrowband filters. For the difficult case of observing well-resolved Mira stars with the H filter at or below 5% visibility level, the limiting magnitude is $H \simeq 4$. The limiting magnitude of the star tracker at IOTA, for these observations, was $V \simeq 12$ for late-type stars. The angular resolution of our short southeast arm at IOTA is lower than that of the northeast arm, meaning that we could miss some asymmetry if it were predominantly parallel to the projected southeast baseline of the interferometer.

Pulsation periods for all Mira and SR variables (53 of 56 program stars) are from the Combined General Catalog of Variable Stars (CGCVS). Among these 53 program stars, 37 also have period estimates from the American Association of Variable Star Observers (AAVSO) derived using a data window centered on JD 2,452,000 (M. R. Templeton et al. 2004, private communication), enabling us to validate the CGCVS periods. In addition, AAVSO has tentative or very tentative periods for three more SR stars. The CGCVS periods are consistent with available AAVSO periods for all but four of our program stars. Interestingly, the AAVSO periods for all four discrepant stars, namely, X Cnc, BG Ser, UU Aur, and W Ori, are roughly twice the CGCVS periods, although the AAVSO periods for two of them, namely, UU Aur and W Ori, are either tentative or very tentative values. For completeness, one of the Irr variables, namely, TX PSc, has a very tentative AAVSO period of 255.5 days.

3. DATA REDUCTION

The recorded interferograms were reduced with an IDL code package developed by one of us (Ragland). Our single-mode integrated-optics beam-combiner chip (Berger et al. 2003) has three input beams (I_a, I_b, and I_c) and six output beams (I_i, $i = 1$–6). Each input is split into two parts and coupled to the outputs

TABLE 1

DERIVED CLOSURE PHASE AND UD DIAMETERS IN THE H BAND FOR TARGETS WITH DETECTED ASYMMETRY

Target	Date (UT)	Calibrator	Calibrator Diameter (mas)	CGCVS Period (days)	AAVSO Period (days)	Phase	Spectral Type	B_{max} (cm)	θ_{UD} (mas)	ϕ_{cp}[e] (deg)
Mira Stars										
IK Tau[c]	2003 Jan 19	63 Ari	2.6	470	...	0.4	M6 e–M10 e	3282.1	24.72 ± 0.23	117.3 ± 1.0
	2003 Jan 29	63 Ari	2.6	470	...	0.4	M6 e–M10 e	3282.3	24.72 ± 0.23	162.4 ± 17.4
	2003 Jan 30	63 Ari	2.6	470	...	0.4	M6 e–M10 e	3309.1	24.72 ± 0.23	152.8 ± 2.9
								3287.0	24.72 ± 0.23	144.4 ± 3.2
R Aur[c]	2003 Jan 19	HD 31312	2.6	457.5	452.5	0.4	M6.5 e–M9.5 e	3461.5	10.01 ± 0.20	−7.0 ± 0.5
	2003 Jan 25	HD 31312	2.6	457.5	452.5	0.4	M6.5 e–M9.5 e	3416.9	10.01 ± 0.20	−6.6 ± 0.6
	2003 Jan 28	HD 31312	2.6	457.5	452.5	0.4	M6.5 e–M9.5 e	3487.0	10.01 ± 0.20	−6.7 ± 0.6
U Ori[c]	2003 Jan 28	40 Ori	2.2	368.3	372.3	0.1	M6 e–M9.5 e	3461.6	11.31 ± 0.41	−8.6 ± 0.6
S CMi	2003 Mar 08	27 Mon	2.4	332.9	329.6	0.4	M7 e	3520.4	7.06 ± 0.08	6.0 ± 0.6
R Cnc[c]	2003 Jan 23	ω Hya	2.5	361.6	362.3	0.3	M6 e–M9 e	3354.7	12.65 ± 0.35	6.7 ± 0.6
								3131.8	12.65 ± 0.35	−1.0 ± 0.7[a]
	2003 Jan 28	ω Hya	2.5	361.6	362.3	0.3	M6 e–M9 e	3424.7	12.65 ± 0.35	9.6 ± 0.7
R LMi[b,c]	2002 Mar 07	ω Hya	2.5	372.2	375.4	0.5	M7 e	2916.8	13.16 ± 0.21	2.6 ± 0.5[a]
	2003 Mar 09	ω Hya	2.5	372.2	375.4	0.5	M7 e	3825.4	13.16 ± 0.21	−5.6 ± 1.2
	2003 Mar 12	ω Hya	2.5	372.2	375.4	0.5	M7 e	3582.7	13.16 ± 0.21	−31.5 ± 0.8
S CrB	2003 Mar 07	HR 5464	2.7	360.3	365	0.5	M7 e	2914.3	8.81 ± 0.16	5.5 ± 0.5
RU Her[b]	2003 Mar 10	51 Her	2.5	484.8	494.1	0.1	M6 e–M9	3823.6	8.00 ± 0.20	−7.2 ± 0.7
	2003 Mar 11	51 Her	2.5	484.8	494.1	0.1	M6 e–M9	3539.3	8.00 ± 0.20	−6.6 ± 0.6
	2003 Mar 13	51 Her	2.5	484.8	494.1	0.1	M6 e–M9	3530.0	8.00 ± 0.20	−11.0 ± 0.7
U Her[c]	2002 Jun 28	κ Ser	6.6	406.1	406.5	0.0	M6.5 e–M9.5 e	3657.9	9.69 ± 0.37	20.9 ± 1.6
R Aql[c]	2002 Jun 27	γ Sge	6.9	284.2	272.9	0.7	M5 e–M9 e	3385.9	12.72 ± 0.20	−26.6 ± 0.8
χ Cyg[c]	2002 May 29	α Vul	5.1	408.1	404.8	0.2	S6, 2e–S10, 4e	2121.9	22.59 ± 0.52	168.7 ± 1.4
R Aqr[c]	2002 Oct 30	ι Cet	4.7	387.0	386.1	0.3	M5 e–M8.5 e+pec	2614.3	19.07 ± 0.08	−11.0 ± 0.9
Semiregular Variables										
UU Aur[c]	2003 Jan 30	HD 61603	2.9	234	(457.5)	...	C5,3–C7,4	3554.4	10.88 ± 0.18	−15.5 ± 0.6
V Hya[b]	2003 Mar 10	α Crt	2.9	530.7	...	0.1	C6, 3e–C7, 5e	2655.2	21.23 ± 2.77[d]	17.4 ± 0.7
	2003 Mar 11	α Crt	2.9	530.7	...	0.1	C6, 3e–C7, 5e	2666.6	21.23 ± 2.77	0.4 ± 0.6[a]
Y CVn[c]	2003 Jan 28	HR 5464	2.7	157	...	...	C5, 4J	3487.7	14.05 ± 0.73	−26.9 ± 1.8
Irregular Variables										
TX PSc[c]	2002 Oct 29	ι Cet	4.7	...	(255.5)	...	C II...	3336.5	9.89 ± 0.17	−4.6 ± 0.7
	2002 Oct 30	ι Cet	4.7	...	(255.5)	...	C II...	3234.3	9.89 ± 0.17	−1.5 ± 0.7[a]

[a] This observation does not show asymmetry.
[b] Observed with the narrowband filter at 1.64 μm.
[c] At least one of the baselines resolved this target to the level of below 5% in V^2.
[d] UD model failed to fit the data. The derived value probably gives the diameter of the dust shell rather than the diameter of the central star.
[e] The uncertainties indicate random errors only (see text).

as follows: $(a, b) \leftrightarrow (1, 2)$; $(a, c) \leftrightarrow (3, 4)$; $(b, c) \leftrightarrow (5, 6)$. The complementary outputs (I_2, I_4, and I_6) have the same information as the normal outputs (I_1, I_3, and I_5) except for a π fringe intensity phase shift. Hence, the normal and the complementary outputs could be combined in order to improve the signal-to-noise ratio of the measurements. The background-subtracted outputs are combined two by two (with opposite signs) and normalized as follows, in order to remove scintillation noise, which is common to both normal and complementary outputs,

$$I_{ab} = \frac{I_1/\bar{I}_1 - I_2/\bar{I}_2}{2}, \tag{1}$$

and correspondingly for the other outputs. Here $\bar{I}$ denotes the mean over the entire scan.

The power spectra of the resulting three outputs I_{ab}, I_{bc}, and I_{ac} are computed, and the fringe power for each of these three outputs is estimated by integrating the power (P) under the fringe profile after background power subtraction (Baldwin et al. 1996). The fringe power is proportional to the visibility squared (V^2). The target $V^2_{\rm targ}$ is calibrated by measuring the fringe power for a nearby calibrator of known $V^2_{\rm cal}$ under the same instrumental configuration and by taking the ratio, i.e.,

$$V^2_{\rm targ} = V^2_{\rm cal}\left(\frac{P_{\rm targ}}{P_{\rm cal}}\right). \tag{2}$$

The closure phase is the sum of the fringe phases simultaneously observed on three baselines forming a closed triangle and is insensitive to phase errors induced by the turbulent atmosphere or optics (Jennison 1958). If the phase errors introduced into the three beams are δ_a, δ_b, and δ_c, then the observed fringe phase between baselines a and b can be written as

$$\phi_{ab} = \psi_{ab} + \delta_b - \delta_a. \tag{3}$$

Here ψ_{ab} is the true object fringe phase between baselines a and b.

TABLE 2

CLOSURE-PHASE MEASUREMENTS FOR TARGETS WITH NO DETECTABLE ASYMMETRIES

Target	Date (UT)	Calibrator	CGCVS Period (days)	AAVSO Period	Phase	Spectral Type	B_{max} (cm)	θ_{UD} (mas)	ϕ_{cp} (deg)
				Mira Stars					
U Per	2002 Oct 30	51 And	320.3	318.7	0.5	M6 e	3607.2	5.84[b]	1.4 ± 1.1
R Tri	2003 Jan 29	24 Per	266.9	264.8	0.9	M4 IIIe	3548.7	4.46[c]	2.8 ± 0.5
RT Eri	2003 Jan 31	HR 1543	370.8	376.5	0.9	M: e	2527.9	6.3[d]	1.0 ± 0.6
R Lep[a]	2003 Jan 31	HR 1543	427.1	437.8	0.8	C IIe...	2904.8	11.50[e]	−3.9 ± 0.6
RU Aur	2003 Jan 29	51 Ori	466.5	464.3	0.7	M8	3553.5	3.7[d]	−0.9 ± 0.6
X Aur	2002 Oct 29	υ Aur	163.8	166.1	0.2	K2	3664.0	1.8[d]	2.5 ± 1.1
	2003 Jan 23	HD 31312	163.8	166.1	0.2	K2	3378.4	1.8[d]	−0.2 ± 0.6
	2003 Jan 25	HD 31312	163.8	166.1	0.2	K2	3429.5	1.8[d]	−0.9 ± 0.6
	2003 Jan 28	HD 31312	163.8	166.1	0.2	K2	3507.5	1.8[d]	−2.1 ± 0.6
V Mon	2003 Jan 29	HD 31312	340.5	332.7	0.2	M6 e	2771.1	5.6[d]	2.6 ± 0.6
W Cnc	2003 Jan 28	ω Hya	393.2	391.8	0.3	M7 e	3415.2	4.7[d]	−0.7 ± 0.6
X Hya	2003 Jan 30	28 Hya	301.1	301.2	0.6	M7 e	2451.7	5.0[d]	−0.2 ± 0.6
R LMi	2003 Jan 28	HR 5464	372.2	375.4	0.3	M7 e	3530.8	13.2[b]	−2.6 ± 0.7
V Boo	2002 May 29	ρ Boo	258.0	261.1	0.6	M6 e	2100.6	5.2[d]	−0.7 ± 0.7
	2003 Jan 28	HR 5464	258.0	261.1	0.6	M6 e	3448.6	5.2[d]	0.2 ± 0.6
S CrB	2002 May 29	52 Boo	360.3	365	0.7	M7 e	2121.3	9.1[b]	0.3 ± 0.8
	2003 Jan 28	HR 5464	360.3	365	0.4	M7 e	3509.1	8.9[b]	1.5 ± 0.6
S Ser	2002 Jun 28	κ Ser	371.8	373.7	0.9	M5 e	3557.1	5.35[f]	−1.3 ± 1.5
BG Ser	2002 Jun 29	κ Ser	143	386.1	0.7	M6 me...	3042.7	6.71[f]	0.1 ± 0.9
	2003 Jan 30	110 Vir	143	386.1	0.3	M6 me...	3328.4	6.71[f]	0.7 ± 0.7
	2003 Jan 30	110 Vir	143	386.1	0.3	M6 me...	3305.8	6.71[f]	−0.2 ± 0.7
R Ser	2002 May 27	κ Ser	356.4	355.6	0.4	M7 IIIe	2089.8	7.6[b]	0.0 ± 1.0
	2002 May 28	κ Ser	356.4	355.6	0.4	M7 IIIe	2052.9	7.6[b]	0.4 ± 0.8
V CrB	2003 Jan 30	HR 5464	357.6	361.3	0.9	N...	3271.8	7.26[e]	−1.5 ± 0.6
RU Her	2002 May 25	HR 5947	484.8	494.1	0.5	M7 e...	2116.5	8.71[f]	1.3 ± 0.9
RT Oph	2002 Jun 28	β Oph	426.3	424.8	0.0	M7	3500.1	6.52[f]	−1.0 ± 1.0
X Oph	2002 May 26	γ Aql	328.9	341.1	0.4	K1 III+...	1968.1	12.97[c]	−0.6 ± 0.8
R Aql	2002 May 26	γ Aql	284.2	272.9	0.5	M7 IIIe	1944.2	9.3[b]	−1.1 ± 0.8
W Aql	2002 May 28	γ Aql	490.4	480.8	0.1	S:...	1650.0	11.08[e]	1.2 ± 1.0
RT Aql	2002 Jun 24	γ Aql	327.1	325.7	0.0	M7 e	3488.8	7.24[f]	1.9 ± 0.8
BG Cyg	2002 Jun 29	γ Sge	228	285.4	0.1	M7 e	3793.5	4.14[f]	−1.8 ± 1.0
RR Aql	2002 May 28	γ Aql	394.8	398.7	1.0	M7 e	1795.9	10.73[f]	0.2 ± 1.0
U Cyg	2002 Jun 28	β Oph	463.2	469	0.0	R...	3732.1	7.05[e]	−3.5 ± 1.4
V1426 Cyg	2002 Oct 30	ρ Cyg	470	481.2	0.9	C	3816.0	10.8[g]	−0.8 ± 0.9
R Peg	2002 Oct 31	7 Psc	378.1	378.2	0.8	M7 e	3579.7	7.0[b]	−1.9 ± 1.2
				Semiregular Variables					
ρ Per	2002 Nov 21	24 Per	50	...	...	M4 II	3825.4	15.53[h]	1.3 ± 3.5
W Ori	2002 Oct 31	40 Ori	212	(446)	...	C II...	3394.3	9.7[g]	5.2 ± 1.8
CE Tau	2002 Oct 30	HD 33554	165	...	...	M2 Iab:	3717.4	9.1[i]	−4.1 ± 1.2
X Cnc	2003 Jan 19	ω Hya	195	379.6	0.3	C II...	3527.5	7.62[j]	1.8 ± 0.6
	2003 Jan 25	ω Hya	195	379.6	0.3	C II...	3473.1	7.62[j]	−0.4 ± 0.6
	2003 Jan 28	ω Hya	195	379.6	0.3	C II...	3410.5	7.62[j]	2.1 ± 0.6
T Cnc	2003 Jan 23	ω Hya	428	499.5	...	N...	3447.1	6.6[k]	−2.0 ± 0.6
	2003 Jan 28	ω Hya	428	499.5	...	N...	3409.6	6.6[k]	0.3 ± 0.6
U Hya	2003 Jan 25	α Crt	450	...	...	C II...	2902.0	10.8[d]	−2.4 ± 0.7
	2003 Jan 30	HR 5464	450	...	...	C II...	2489.6	10.8[d]	−2.8 ± 0.6
V Hya	2003 Jan 23	α Crt	530.7	...	1.0	C...	2640.1	13.0[d]	2.1 ± 0.6
Y CVn	2002 May 29	HR 4690	157	...	...	C Iab:...	2022.7	11.6[g]	−3.6 ± 1.0
RT Vir	2002 May 28	υ Boo	155	...	...	M8 III	1902.3	12.38[l]	0.7 ± 0.7
SW Vir	2002 May 28	υ Boo	150	155.4	...	M7 III	1818.9	16.24[l]	2.8 ± 0.9
RX Boo[a]	2002 May 23	ρ Boo	340	...	...	M7.5	2112.2	17.48[l]	−3.9 ± 1.0
ST Her	2002 May 23	HR 5763	148	...	...	M6 s	1945.5	9.3[m]	−0.1 ± 1.0
X Her	2002 May 25	HR 5763	95	...	...	M	1989.5	12.1[m]	0.0 ± 1.0
g Her[a]	2002 May 29	52 Boo	89.2	...	...	M6 III	2063.0	12.67[l]	−2.5 ± 1.0
R Lyr[a]	2002 May 25	HR 6695	46	...	...	M5 III	2056.4	13.3[m]	0.3 ± 0.9
V Aql	2002 Jun 28	β Oph	353	377.1	...	C II...	2870.1	10.1[g]	−0.8 ± 1.0
EU Del	2002 May 26	γ Sge	59.7	...	0.7	M6 III	2063.7	9.8[i]	−0.8 ± 0.8

TABLE 2—*Continued*

Target	Date (UT)	Calibrator	CGCVS Period (days)	AAVSO Period	Phase	Spectral Type	B_{max} (cm)	θ_{UD} (mas)	ϕ_{cp}[o] (deg)
				Irregular Variables					
Del2 Lyr	2002 May 25	HR 6695	...	...	...	M4 II	2099.3	10.32[n]	-0.6 ± 0.9
EPS Peg	2002 Jun 25	7 Peg	...	...	...	K2 Ib	3657.3	7.7[m]	-0.1 ± 1.1
TX PSc[a]	2002 Jun 25	7 Peg	...	(255.5)	...	C II...	3571.0	11.2[g]	4.9 ± 1.6

[a] At least one of the baselines resolves this target to the level of below 5% in V^2.
[b] Millan-Gabet et al. (2005).
[c] Thompson et al. (2002).
[d] Van Belle (1999).
[e] Van Belle et al. (1997).
[f] Van Belle et al. (2002).
[g] Dyck et al. (1996b).
[h] Di Benedetto (1993).
[i] Dyck et al. (1998).
[j] Richichi & Calamai (2003).
[k] Richichi et al. (1991).
[l] Mennesson et al. (2002).
[m] Dyck et al. (1996a).
[n] Sudol et al. (2002).
[o] The uncertainties indicate random errors only (see text).

The observed closure phase Φ_{cl} is equal to the true object closure phase, $\psi_{ab} + \psi_{bc} + \psi_{ca}$, to within the measurement noise, as follows:

$$\Phi_{cl} = \phi_{ab} + \phi_{bc} + \phi_{ca} + \text{noise} \quad (4)$$

$$= \psi_{ab} + \delta_b - \delta_a + \psi_{bc} + \delta_c - \delta_b + \psi_{ca} + \delta_a - \delta_c + \text{noise} \quad (5)$$

$$= \psi_{ab} + \psi_{bc} + \psi_{ca} + \text{noise}. \quad (6)$$

We estimate closure phase as the phase of the bispectrum (Weigelt 1977) of simultaneous fringes obtained with the three baselines. The instrumental closure phase is estimated using a nearby calibrator and subtracted from the raw closure phase of the target to give a calibrated target closure phase.

Typical 1 σ formal errors in our uncalibrated closure-phase and V^2 measurements are $\sim 0.^\circ 2$ and $\sim 2\%$, respectively. The formal errors are estimated from the scatters of the 500 fringe scans. In the case of V^2 errors, the error due to background power subtraction is also incorporated into the formal error. The calibration process adds up additional errors, and the measurement error is estimated as the square root of the sum of the squares of the formal and calibration errors. The 1 σ measurement error is reported in Tables 1 and 2. We estimate calibration errors by observing calibrators under the same observing conditions and calibrating one calibrator with the other after accounting for the finite sizes of both calibrators. The estimated 1 σ calibration error is 5% for the V^2 measurements and $0.^\circ 5$ for closure-phase measurements. There could be unaccounted for systematic errors in our measurements. For the purposes of this paper, we adopt a systematic error of 2° for our closure-phase measurements. The total error is estimated as the square root of the sum of the squares of the formal, calibration, and systematic errors. If the measured closure phase is less than twice the total error in the measurement, then we call it essentially a nondetection of asymmetry. However, if it is larger, we call it a positive detection. Further discussion on our visibility and closure-phase measurements can be found in Ragland et al. (2004).

4. RESULTS

Targets with centrosymmetry should give a closure phase of either zero or $\pm 180^\circ$ depending on how many baselines are beyond the first, second, etc., nulls. The majority of our targets show zero closure phase. However, 16 of the 56 have nonzero closure phase. Of these, 12 are Mira stars and 4 are SR/Irr variable carbon stars. Among the 12 Mira stars, all but χ Cyg are oxygen-rich Mira stars; χ Cyg is classified as an S star. The frequency of asymmetry from our studies is 34% in Mira stars, 17% in SR variables, 33% in Irr variables, and thus 29% in our entire sample of AGB stars. In terms of chemistry, the frequency of asymmetry is 33% in carbon stars and 27% in oxygen-rich stars.

Table 1 gives the measured closure phases along with observational and target information for these 16 targets that show measurable asymmetry from our observations. We have included in this table one observation each for R Cnc, R LMi, and V Hya, in which no asymmetry is detected, since we use these observations for size estimation. All targets (except R Aur, χ Cyg, and UU Aur) have follow-up measurements taken with all three narrowband filters to characterize the observed asymmetry. These results will be presented elsewhere. The V^2 data for these targets are fitted with uniform disk (UD) models (Fig. 1), and the measured angular sizes are also given in Table 1. Table 2 lists targets for which we have not detected asymmetry from our survey. The calibrators used for our observations are also listed in these tables. The angular sizes for most of the calibrators are taken from Wesselink et al. (1972). Typically, we use calibrators with angular sizes less than 3 mas for our measurements. However, during the early part of the survey, we had to use larger calibrators because of low throughput of the instrument. We adopted the measured sizes from interferometric techniques for α Vul and γ Sge (Hutter et al. 1989) and from lunar occultation measurements for UU Aur (Bohme 1978). We estimated the angular size of 7 Peg from V and K magnitudes (van Belle 1999).

Six of our targets with detected asymmetry, namely, U Ori, R Cnc, R LMi, S CrB, R Aql, and R Aqr, have earlier H-band size measurements (Millan-Gabet et al. 2005) taken within ± 0.2 pulsation phase with respect to the pulsation phase of our measurements for these stars. We have plotted our size measurements against the measurements by these authors for these six targets in Figure 2. The scatter in this figure is comparable to the scatter among measurements of a given star at multiple epochs in a single program and thus probably signifies either actual size variation at the source or that the interpretation of the observations

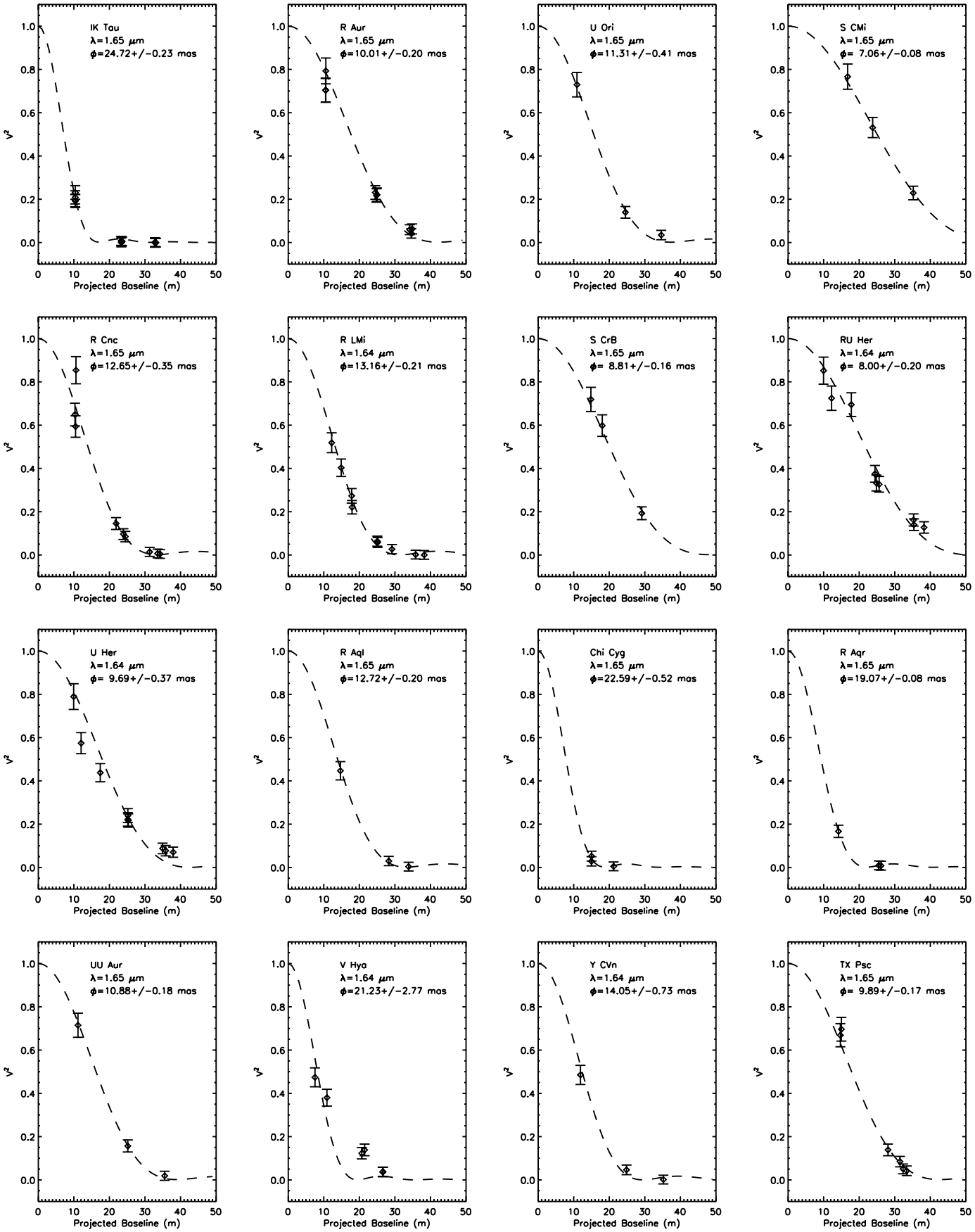

FIG. 1.— Visibility data fitted with a UD model for the targets with positive asymmetry detection from our observations. UD models fit the data very well except for V Hya. In the case of V Hya, the derived size is possibly the size of the dust shell rather than that of the central star. [*See the electronic edition of the Journal for a color version of this figure.*]

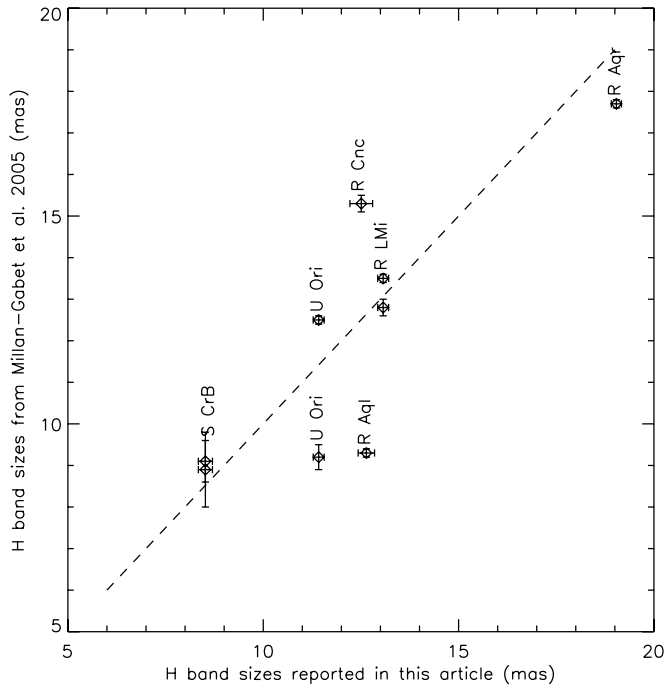

FIG. 2.—Comparison of sizes reported in this paper with those reported in the literature.

(UD) is too simple. Several targets have earlier *K*-band angular size measurements (van Belle et al. 1996, 2002; Millan-Gabet et al. 2005; Mennesson et al. 2002; Dyck et al. 1996b).

Of 56 AGB stars, 16 are well resolved (i.e., at least one baseline gives a V^2 measurement less than 5% of the point-source value) by our observations. Among these 16 targets, 12 show asymmetry from our observations. Thus, if we consider only well-resolved targets, 75% of AGB stars show asymmetry. Targets from our measurements that are well resolved are marked in Tables 1 and 2 (see Table 1 footnote c and Table 2 footnote a). Interestingly, all well-resolved targets that do not show asymmetry (except R Lep), namely, g Her, R Lyr, and RX Boo, are SR variables; R Lep is a carbon Mira variable. Thus, if we consider only well-resolved oxygen-rich Mira stars, then our asymmetry detection is 100% and in the case of SR variables the success rate is 40%. The well-resolved Mira variable R LMi did not show asymmetry from our 2003 January observations. However, we detected asymmetry in this target during 2003 March observations. Similarly, the well-resolved Irr variable TX Psc did not show asymmetry from our 2002 June measurements. However, we detected asymmetry in TX Psc from our follow-up observations taken in 2002 October.

At least five targets with detected asymmetry, namely, S CrB, RU Her, R Aql, V Hya, and Y CVn, have earlier measurements taken with relatively shorter baselines, and we did not detect asymmetry from these measurements.

In order to understand the role of angular resolution in the asymmetry detection, we derived the number of pixel elements ($N_{\rm pix}$) in an imaging sense, defined as the angular diameter divided by the angular resolution ($\lambda/2B_{\rm max}$) for all targets. Here $B_{\rm max}$ is the maximum baseline of our observations listed in Tables 1 and 2 for all our targets. We plotted our measured closure-phase values against the number of pixel elements in Figure 3. This figure clearly shows that the positive closure-phase cases are those that have pixel elements close to or greater than unity, meaning that they are well resolved. This suggests that the detected asymmetry features are probably on the surface of the stellar disk or visible only in projection against the stellar disk (such as might be the case for patchy dust opacity at 1.5–2.5 stellar radii).

5. SIMPLE MODELS

We have assumed a two-component brightness distribution model in order to find the simplest possible implications of the measured closure-phase signal. This model consists of a uniform-disk star with an intensity distribution $\tilde{I}_p(\boldsymbol{r})$ and an unresolved secondary component (bright spot, companion, or dust clump) with an intensity distribution $\tilde{I}_s(\boldsymbol{r}-\delta\boldsymbol{r})$, where $\delta\boldsymbol{r}$ is the separation vector between the optical centers of the components. The total intensity is $I=\tilde{I}_p(\boldsymbol{r})+\tilde{I}_s(\boldsymbol{r}-\delta\boldsymbol{r})$. The complex visibility is the Fourier transform of the brightness distribution. Thus, the complex visibility of this composite object could be written using the shift theorem for Fourier transforms as

$$\hat{V}(\boldsymbol{g})=\hat{V}^p(\boldsymbol{g})+\hat{V}^s(\boldsymbol{g})e^{ik\boldsymbol{g}\cdot\delta\boldsymbol{r}}, \tag{7}$$

where $k=2\pi/\lambda$, λ is the wavelength of observation, and $\boldsymbol{g}$ is the baseline vector $\boldsymbol{B}$.

The complex visibility for the baseline $\boldsymbol{B}_{AB}$ could be written as

$$\hat{V}_{AB}=V^p_{AB}e^{i\phi^p_{AB}}+V^s_{AB}e^{i\phi^s_{AB}}e^{ik\boldsymbol{B}_{AB}\cdot\delta\boldsymbol{r}}. \tag{8}$$

The visibility phase for the baseline B_{AB} is

$$\phi_{AB}=\arctan\left(\frac{\mathrm{Im}\,\hat{V}_{AB}}{\mathrm{Re}\,\hat{V}_{AB}}\right) \tag{9}$$

$$=\arctan\left[\frac{V^p_{AB}\sin\phi^p_{AB}+V^s_{AB}\sin(\phi^s_{AB}+k\boldsymbol{B}_{AB}\cdot\delta\boldsymbol{r})}{V^p_{AB}\cos\phi^p_{AB}+V^s_{AB}\cos(\phi^s_{AB}+k\boldsymbol{B}_{AB}\cdot\delta\boldsymbol{r})}\right] \tag{10}$$

$$=\arctan\Bigg\{\left[V^p_{AB}\sin\phi^p_{AB}+V^s_{AB}\sin\phi^s_{AB}\cos(k\boldsymbol{B}_{AB}\cdot\delta\boldsymbol{r})+V^s_{AB}\cos\phi^s_{AB}\sin(k\boldsymbol{B}_{AB}\cdot\delta\boldsymbol{r})\right]\times\left[V^p_{AB}\cos\phi^p_{AB}+V^s_{AB}\cos\phi^s_{AB}\cos(k\boldsymbol{B}_{AB}\cdot\delta\boldsymbol{r})-V^s_{AB}\sin\phi^s_{AB}\sin(k\boldsymbol{B}_{AB}\cdot\delta\boldsymbol{r})\right]^{-1}\Bigg\}. \tag{11}$$

The individual components of the brightness distributions are assumed to be circularly symmetric. Hence, $\sin(\phi^p_{AB})=\sin(\phi^s_{AB})=0$, but $\cos(\phi^p_{AB})$ and $\cos(\phi^s_{AB})$ can be +1 or −1, depending on details of the case. Thus,

$$\phi_{AB}=\arctan\Bigg\{\left[V^s_{AB}\cos\phi^s_{AB}\sin(k\boldsymbol{B}_{AB}\cdot\delta\boldsymbol{r})\right]\times\left[V^p_{AB}\cos\phi^p_{AB}+V^s_{AB}\cos\phi^s_{AB}\cos(k\boldsymbol{B}_{AB}\cdot\delta\boldsymbol{r})\right]^{-1}\Bigg\}. \tag{12}$$

Unresolved secondary component.—For an unresolved component (i.e., a point source) $\phi^s_{AB}=0$. Thus,

$$\phi_{AB}=\arctan\left[\frac{V^s_{AB}\sin(k\boldsymbol{B}_{AB}\cdot\delta\boldsymbol{r})}{V^p_{AB}\cos\phi^p_{AB}+V^s_{AB}\cos(k\boldsymbol{B}_{AB}\cdot\delta\boldsymbol{r})}\right]. \tag{13}$$

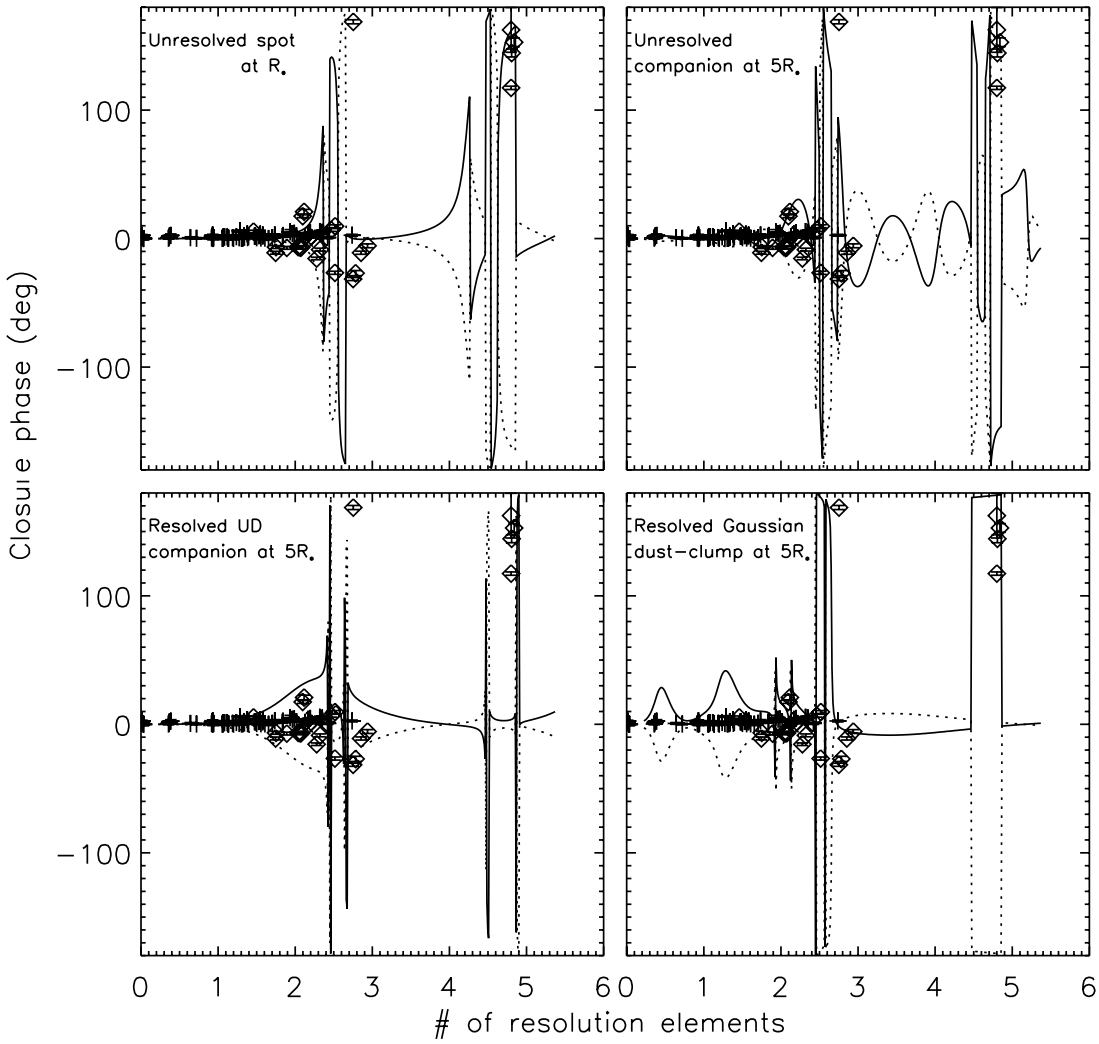

FIG. 3.—Measured closure phases vs. number of pixel elements (see text). Targets with positive asymmetry detection (*diamonds*) and nondetection (*plus signs*) measurements are shown. Targets that are well resolved frequently show large closure phase. The solid lines refer to models in which the secondary feature is assumed at a position angle of 21°.8 (along the direction of the largest baseline of the IOTA array), and the dotted lines refer to models where the secondary feature is assumed at a position angle of 201°.8 (21°.8 + 180°). The flux of the unresolved secondary components is assumed to be 3%, and that of the resolved secondary component is assumed to be 30%. *Top left,* Unresolved spot at the edge of the stellar disk ($\delta r = \theta_{\rm UD}/2$); *top right*, unresolved companion at five stellar radii ($\delta r = 2.5\theta_{\rm UD}$); *bottom left*, resolved UD companion at five stellar radii ($\delta r = 2.5\theta_{\rm UD}$; the diameter of the secondary is assumed to be 99% of the diameter of the primary); *bottom right*, resolved Gaussian dust clump at five stellar radii ($\delta r = 2.5\theta_{\rm UD}$; the equivalent size of the secondary is assumed to be same as that of the primary).

For a uniform-disk star,

$$\hat{V}^p_{AB} = \left[\frac{2J_1(\pi N^{AB}_{\rm pix}/2)}{\pi N^{AB}_{\rm pix}/2}\right] I_p, \tag{14}$$

and

$$V^p_{AB}\cos\phi^p_{AB} = \left[\frac{2J_1(\pi N^{AB}_{\rm pix}/2)}{\pi N^{AB}_{\rm pix}/2}\right] I_p. \tag{15}$$

For an unresolved secondary component,

$$V^s_{AB} = I_s, \tag{16}$$

where I_p and I_s are the normalized star and secondary component intensities (i.e., $I_p + I_s = 1$), and

$$N^{AB}_{\rm pix} = \frac{\theta_{\rm UD}}{\lambda/2B_{AB}}. \tag{17}$$

Combining equations (13), (15), and (16), we get

$$\phi_{AB} = \arctan\left(\left[I_s \sin\left(k\boldsymbol{B}_{AB}\cdot\delta\boldsymbol{r}\right)\right] \times\left\{I_p\left[\frac{2J_1(\pi N^{AB}_{\rm pix}/2)}{\pi N^{AB}_{\rm pix}/2}\right] + I_s\cos\left(k\boldsymbol{B}_{AB}\cdot\delta\boldsymbol{r}\right)\right\}^{-1}\right). \tag{18}$$

Resolved secondary component.—For a resolved Gaussian secondary component (such as a dust clump) $\phi^s_{AB} = 0$, and

$$V^s_{AB} = \left[\exp -\left(\frac{\pi\beta N^{AB}_{\rm pix}}{2\alpha}\right)^2\right] I_s, \tag{19}$$

where $\alpha = 2\sqrt{\ln 2}$ and β is the ratio of the size of the primary component to the secondary.

Thus,

$$\phi_{AB} = \arctan\left(\left[I_s \exp -\left(\frac{\pi\beta N_{\rm pix}^{AB}}{2\alpha}\right)^2 \sin\left(k\boldsymbol{B}_{AB}\cdot\delta\boldsymbol{r}\right)\right] \times\left\{I_p\left[\frac{2J_1(\pi N_{\rm pix}^{AB}/2)}{\pi N_{\rm pix}^{AB}/2}\right] + I_s \exp -\left(\frac{\pi\beta N_{\rm pix}^{AB}}{2\alpha}\right)^2 \cos\left(k\boldsymbol{B}_{AB}\cdot\delta\boldsymbol{r}\right)\right\}^{-1}\right). \quad (20)$$

For a resolved uniform-disk secondary component (such as a stellar companion) $\phi_{AB}^s = 0$ or $\pm\pi$, and

$$\hat{V}_{AB}^s = \left[\frac{2J_1(\pi\beta N_{\rm pix}^{AB}/2)}{\pi\beta N_{\rm pix}^{AB}/2}\right] I_s, \quad (21)$$

$$V_{AB}^s \cos\phi_{AB}^s = \left[\frac{2J_1(\pi\beta N_{\rm pix}^{AB}/2)}{\pi\beta N_{\rm pix}^{AB}/2}\right] I_s. \quad (22)$$

Now

$$\phi_{AB} = \arctan\left(\left\{I_s\left[\frac{2J_1(\pi\beta N_{\rm pix}^{AB}/2)}{\pi\beta N_{\rm pix}^{AB}/2}\right] \sin\left(k\boldsymbol{B}_{AB}\cdot\delta\boldsymbol{r}\right)\right\} \times\left\{I_p\left[\frac{2J_1(\pi N_{\rm pix}^{AB}/2)}{\pi N_{\rm pix}^{AB}/2}\right] + I_s\left[\frac{2J_1(\pi\beta N_{\rm pix}^{AB}/2}{\pi\beta N_{\rm pix}^{AB}/2}\right] \cos\left(k\boldsymbol{B}_{AB}\cdot\delta\boldsymbol{r}\right)\right\}^{-1}\right). \quad (23)$$

Using equations (4), (18), (20), and (23), we generate closure-phase models for the IOTA configuration A35B15C00 (i.e., $B_{CA} =$ 35 m; $B_{BC} = 15$ m), which are shown with our data in Figure 3. We explored the parametric space with four cases, namely, (1) surface-unresolved spot, (2) surface-unresolved companion, (3) surface-resolved companion, and (4) surface-resolved Gaussian dust clump. The values assumed for various parameters of these models are primarily for the purpose of illustration. A more thorough treatment of the physical parameters chosen in the models will be presented in a forthcoming paper. We have shown two models for each of the four cases (eight models in total) in Figure 3. The two models differ only in the position angle of the secondary feature—one assumes the secondary feature at a position angle of 21.°8 and the other at a position angle of 201.°8 (i.e., a 180° rotation). The reason for choosing this axis (along the direction of the largest baseline of the IOTA array) is that the closure-phase signal is approximately maximum when the secondary feature is assumed along this axis. The brightness distribution of the primary component is assumed to be a uniformly illuminated disk. The flux of the secondary component is assumed to be 3% of the total flux for surface-unresolved secondary cases and 30% for surface-resolved secondary component cases; the reason for choosing these flux values for the companion is that the corresponding models compare well with our closure-phase measurements. The spot models (case 1) assume a surface-unresolved bright spot at the edge of the stellar disk ($\delta r = \theta_{\rm UD}/2$). The surface-unresolved binary models (case 2) assume a surface-unresolved companion or dust clump at five stellar radii ($\delta r = 2.5\theta_{\rm UD}$). The surface-resolved binary models (case 3) assume a companion with $\beta = 0.99$ (UD angular size of the secondary component is 99% of the primary) at five stellar radii ($\delta r = 2.5\theta_{\rm UD}$). If companion stars provide enough light to produce detectable asymmetry near maximum light, then they should also produce wider, flattened minima in the light curves (Merrill 1956). While at least two of the stars are known binaries and relatively mild symbiotic systems (R Aqr and *o* Ceti), none of the stars show a filled-in minimum on the AAVSO light curves. The dust models (case 4) assume a Gaussian-shaped dust clump ($\beta = 1$; same equivalent size as the primary component) at five stellar radii ($\delta r = 2.5\theta_{\rm UD}$). As can be seen in Figure 3, the unresolved spot models compare well with the observed data and the unresolved companion models are not as good as the unresolved spot models in explaining the observed closure-phase data. The resolved secondary feature models (cases 3 and 4) show that the secondary components have to be significantly brighter (which may be physically unreasonable) in order to produce detectable closure-phase signals, and even so, the fits at low $N_{\rm pix}$ are poor.

6. DISCUSSION

The significance of our results (i.e., that $\frac{1}{3}$ are asymmetric and $\frac{2}{3}$ are not) depends on what causes the asymmetry, and that is not yet known. As noted in § 1, although planetary nebulae are predominantly bipolar, a large fraction (possibly even all) of proto-PNe are axisymmetric inside an apparently spherical AGB wind remnant, suggesting that the PN asymmetry has arisen only after or as the star left the AGB. Asymmetries have been reported before for Mira variables, but these are mostly for isolated examples, or for maser emission that is very sensitive to the local conditions and thus will tend to exaggerate any physical departure from spherically symmetric flow. Our results, referring to intensity near the stellar flux maximum, are much less sensitive to small variations in the conditions. It is worth mentioning here that the nondetections do not preclude asymmetries. It could be that they are just not resolved or the asymmetries are too small.

The SiO maser emission also arises well above the photosphere (e.g., Humphreys et al. 2002; Cotton et al. 2004); in fact, there is, to our knowledge, no report yet of asymmetry that can be assigned unambiguously to the stellar surface. With multiple narrowband measurements at carefully selected wavelengths, Perrin et al. (2004) have shown that it is possible to disentangle photospheric and shell contributions. The results reported here suggest that we will also be able to sort out some shape information in the next generation of observations, as well as separate the photospheric contribution from the circumstellar one.

There is a considerable literature concerning the noncircular and nonspherical symmetry common among planetary nebulae; see, for example, the proceedings of Asymmetric Planetary Nebulae III (Meixner et al. 2004). Mechanisms can be roughly divided into deep and superficial. Deep mechanisms include internal convective structure with large convection cells (proposed by Schwarzschild [1975] on the basis of simple scaling arguments), nonradial pulsation, and/or rotation.

These stars have massive envelopes and large radii; no reasonable reservoir of angular momentum other than incorporation of a relatively massive (>0.1 $M_\odot$) companion will provide sufficient angular momentum for rotational asymmetry or the usual nonradial pulsation associated with rotation. Large convective cells might stimulate nonradial modes in the absence of significant rotation or might lead to modulations in the surface brightness

from rising or falling elements. Evolutionary models show a radiative layer above the convective layer in these stars (Ostlie & Cox 1986), and the scale heights at the photosphere are only $\sim 0.01 R_*$; these facts suggest that convective modulation will be on a smaller scale and with less contrast than is needed to explain these observations, but more detailed modeling should be done before the possibility of convection-based modulation is ruled out.

Superficial or atmospheric mechanisms include magnetic structures (e.g., Soker & Zoabi 2002; Blackman et al. 2001), discrete dust cloud formation as for R CrB stars, and interaction of a planet or companion with the stellar wind (Struck et al. 2004; Mastrodemos & Morris 1998, 1999). The conclusion that perhaps all of the Mira variables show some asymmetry while only about half of the non-Mira variables do can be understood in a couple of ways. Mira variables comprise a well-defined subset of long-period variables, namely, those with large visual amplitudes, relatively regular variation, cool effective temperatures, and moderate progenitor masses. SR classes differ in visual amplitude (SRa), degree of irregular variation (SRb), warmer effective temperature (SRd), and higher progenitor mass (SRc). Within each of these classes there are further probable subclasses. Our current understanding is that the high visual amplitude is partly the result of variable atmospheric opacity (Reid & Goldston 2002); this variable opacity is closely tied to the fact that these stars are losing mass at a high rate ($>10^{-7}\,M_\odot\,\mathrm{yr}^{-1}$ up to $10^{-5}\,M_\odot\,\mathrm{yr}^{-1}$) so the evolutionary status of Mira variables is that they are stars entering the final "superwind" (massive outflow) stage on the AGB (e.g., review by Willson 2000). A number of stars initially classified as Mira variables are reclassified as SRb when their light curves develop irregularities, making the boundary between these two classes somewhat fuzzy. Similarly, most relatively regular carbon star long-period variables have smaller amplitudes in the visual than do the oxygen-rich stars, and this may be telling us more about the sources of atmospheric opacity than about the evolutionary state, so the SRa-Mira boundary is also fuzzy. Thus, one interpretation would be that the asymmetry shows up when there is a sufficiently massive outflow to produce the large Mira amplitude for the oxygen-rich stars and that the SR variables with asymmetries are those with different visual opacity but similarly massive outflows. Either the same mechanism leads to outflow and asymmetry (e.g., nonradial pulsation) or the outflow sets up conditions for asymmetry to be seen. In the first case, the nonradial structure originates at the photosphere; in the second, with aperiodicities in the outflow.

Most Mira variables are surrounded by translucent "molecular shells," a locus in the outflow where molecules and probably dust provide high local opacity, whose IR and visual optical depth is on the order of 1 (0.1 to several; Perrin et al. 2004). The physics of dust formation in the context of large-amplitude pulsation and consequent shocks is reviewed in Willson (2000). Dust grains nucleated in the refrigerated zone between shocks may require several pulsation cycles to grow to sufficient size to generate an outflow, and this would naturally lead to critical dust levels appearing in different cycles at different positions around the star. Whether by this or another mechanism, the translucent shell is likely to have a patchy opacity, allowing more of the photospheric light through in some places than in others. Thus, a plausible explanation for the possibly universal asymmetry in Mira variables would be the formation of an inhomogeneous translucent molecular screen around 1.5–2.5 stellar radii.

In conclusion, we carried out a survey of AGB stars with the IOTA three-telescope imaging interferometer at near-infrared wavelengths, searching for asymmetry in their flux distributions. We find that 29% of our sample show asymmetry. If we restrict the sample to only well-resolved targets, then 75% of AGB stars and 100% of oxygen-rich Mira stars show asymmetry from our observations. On this basis, we hypothesize that all Mira stars might show detectable asymmetry if observed with adequate spatial resolution. The large frequency of asymmetry reported here suggests that angular size measurements and limb-darkening studies of AGB stars carried out with two-telescope optical long-baseline interferometers should be interpreted with caution. We have initiated a systematic mapping program, namely, The Mira Imaging Project funded by the National Science Foundation (NSF) at the IOTA, ISI, and VLBA interferometers to connect the asymmetry in space and time and pinpoint the mechanism(s) responsible for observed asymmetry.

This work was performed in part under contract with the Jet Propulsion Laboratory (JPL) through a Michelson Postdoctoral Fellowship to S. Ragland, funded by NASA as an element of the Navigator (planet finder) Program. JPL is managed for NASA by the California Institute of Technology. We acknowledge support from the NSF through research grants AST 01-38303 and AST 04-56047. The IOTA is principally supported by the Smithsonian Astrophysical Observatory and the University of Massachusetts. The National Radio Astronomy Observatory (NRAO) is operated by Associated Universities, Inc., under cooperative agreement with the NSF. We thank the referee for constructively critical comments that have helped us to significantly improve the paper. This research has made use of NASA's Astrophysics Data System Bibliographic Services and AAVSO's database for light curves.

REFERENCES

Allen, D. A. 1984, Ap&SS, 99, 101
Baldwin, J. E., et al. 1996, A&A, 306, L13
Belczyński, K., Mikołajewska, J., Munari, U., Ivison, R. J., & Friedjung, M. 2000, A&AS, 146, 407
Berger, J.-P., et al. 2003, Proc. SPIE, 4838, 1099
Blackman, E. G., Frank, A., Markiel, J. A., Thomas, J. H., & Van Horn, H. M. 2001, Nature, 409, 485
Bohme, D. D. 1978, Astron. Nachr., 299, 243
Bowen, G. H., & Willson, L. A. 1991, ApJ, 375, L53
Brocksopp, C., Sokoloski, J. L., Kaiser, C., Richards, A. M., Muxlow, T. W. B., & Seymour, N. 2004, MNRAS, 347, 430
Cotton, W. D., et al. 2004, A&A, 414, 275
Diamond, P. J., & Kemball, A. J. 2003, ApJ, 599, 1372
Diamond, P. J., Kemball, A. J., Junor, W., Zensus, A., Benson, J., & Dhawan, V. 1994, ApJ, 430, L61
Di Benedetto, G. P. 1993, A&A, 270, 315
Dyck, H. M., Benson, J. A., van Belle, G. T., & Ridgway, S. T. 1996a, AJ, 111, 1705
Dyck, H. M., van Belle, G. T., & Benson, J. A. 1996b, AJ, 112, 294
Dyck, H. M., van Belle, G. T., & Thompson, R. R. 1998, AJ, 116, 981
Frogel, J. A., Persson, S. E., & Cohen, J. G. 1981, ApJ, 246, 842
Greenhill, L. J., Colomer, F., Moran, J. M., Backer, D. C., Danchi, W. C., & Bester, M. 1995, ApJ, 449, 365
Haniff, C. A., Ghez, A. M., Gorham, P. W., Kulkarni, S. R., Matthews, K., & Neugebauer, G. 1992, AJ, 103, 1662
Hinkle, K. H., Scharlach, W. W. G., & Hall, D. N. B. 1984, ApJS, 56, 1
Hofmann, K.-H., Balega, Y., Scholz, M., & Weigelt, G. 2000, A&A, 353, 1016
Humphreys, E. M. L., Gray, M. D., Yates, J. A., Field, D., Bowen, G. H., & Diamond, P. J. 2002, A&A, 386, 256
Hutter, D. J., et al. 1989, ApJ, 340, 1103
Imai, H., Obara, K., Diamond, P. J., Omodaka, T., & Sasao, T. 2002, Nature, 417, 829
Jennison, R. C. 1958, MNRAS, 118, 276
Karovska, M., Hack, W., Raymond, J., & Guinan, E. 1997, ApJ, 482, L175
Karovska, M., Nisenson, P., Papaliolios, C., & Boyle, R. P. 1991, ApJ, 374, L51

Kellogg, E., Pedelty, J. A., & Lyon, R. G. 2001, ApJ, 563, L151
Knapp, G. R., & Morris, M. 1985, ApJ, 292, 640
Kraus, S., & Schloerb, F. P. 2004, Proc. SPIE, 5491, 56
Lattanzi, M. G., Munari, U., Whitelock, P. A., & Feast, M. W. 1997, ApJ, 485, 328
Lopez, B., et al. 1997, ApJ, 488, 807
Luthardt, R. 1992, Rev. Mod. Astron., 5, 38
Mastrodemos, N., & Morris, M. 1998, ApJ, 497, 303
———. 1999, ApJ, 523, 357
Meixner, M., et al. 2004, ASP Conf. Ser. 313, Asymmetrical Planetary Nebulae III: Winds, Structure and the Thunderbird (San Francisco: ASP)
Mennesson, B., et al. 2002, ApJ, 579, 446
Merrill, P. W. 1956, PASP, 68, 162
Millan-Gabet, R., Pedretti, E., Monnier, J. D., Schloerb, F. P., Traub, W. A., Carleton, N. P., Lacasse, M. G., & Segransan, D. 2005, ApJ, 620, 961
Monnier, J. D., Tuthill, P. G., & Danchi, W. C. 2000, ApJ, 545, 957
Monnier, J. D., et al. 2004a, ApJ, 602, L57
———. 2004b, ApJ, 605, 436
Mozurkewich, D., & Armstrong, J. T. 1992, in ESO Conf. Proc. 39, High-Resolution Imaging by Interferometry II, ed. J. M. Beckers & F. Merkle (Garching: ESO), 801
Ostlie, D. A., & Cox, A. N. 1986, ApJ, 311, 864
Pedretti, E., et al. 2004, PASP, 116, 377
———. 2005, Appl. Opt., 44, 5173
Perrin, G., et al. 2004, A&A, 426, 279
Ragland, S. 1996, Ph.D. thesis, Physical Research Laboratory, India
Ragland, S., et al. 2004, Proc. SPIE, 5491, 1390
Reid, M. J., & Goldston, J. E. 2002, ApJ, 568, 931
Reimers, D., & Cassatella, A. 1985, ApJ, 297, 275
Richichi, A., & Calamai, G. 2003, A&A, 399, 275
Richichi, A., Chandrasekhar, T., Lisi, F., Howell, R. R., Meyer, C., Rabbia, Y., Ragland, S., & Ashok, N. M. 1995, A&A, 301, 439
Richichi, A., Lisi, F., & Calamai, G. 1991, A&A, 241, 131
Sahai, R., Morris, M., Knapp, G. R., Young, K., & Barnbaum, C. 2003, Nature, 426, 261
Samus, N. N., et al. 2004, Combined General Catalog of Variable Stars (Moscow: Inst. Astron. Russian Acad. Sci. and Sternberg State Astron. Inst. Moscow State Univ.)
Schwarzschild, M. 1975, ApJ, 195, 137
Soker, N., & Zoabi, E. 2002, MNRAS, 329, 204
Sokoloski, J. L., & Kenyon, S. J. 2003, ApJ, 584, 1021
Soria-Ruiz, R., Alcolea, J., Colomer, F., Bujarrabal, V., Desmurs, J.-F., Marvel, K. B., & Diamond, P. J. 2004, A&A, 426, 131
Struck, C., Cohanim, B. E., & Willson, L. A. 2004, MNRAS, 347, 173
Su, K. Y. L. 2004, in ASP Conf. Ser. 313, Asymmetrical Planetary Nebulae III: Winds, Structure and the Thunderbird, ed. M. Meixner et al. (San Francisco: ASP), 247
Sudol, J. J., Benson, J. A., Dyck, H. M., & Scholz, M. 2002, AJ, 124, 3370
Thompson, R. R., Creeck-Eakman, M. J., & Akeson, R. L. 2002, ApJ, 570, 373
Traub, W. A., et al. 2004, Proc. SPIE, 5491, 482
Tuthill, P. G., Danchi, W. C., Hale, D. S., Monnier, J. D., & Townes, C. H. 2000, ApJ, 534, 907
Tuthill, P. G., Haniff, C. A., & Baldwin, J. E. 1997, MNRAS, 285, 529
———. 1999, MNRAS, 306, 353
van Belle, G. T. 1999, PASP, 111, 1515
van Belle, G. T., Dyck, H. M., Benson, J. A., & Lacasse, M. G. 1996, AJ, 112, 2147
van Belle, G. T., Dyck, H. M., Thompson, R. R., Benson, J. A., & Kannappan, S. J. 1997, AJ, 114, 2150
van Belle, G. T., Thompson, R. R., & Creech-Eakman, M. J. 2002, AJ, 124, 1706
Weigelt, G., Balega, Y., Hofmann, K.-H., & Scholz, M. 1996, A&A, 316, L21
Weigelt, G. P. 1977, Opt. Commun., 21, 55
Weiner, J., et al. 2006, ApJ, 636, 1067
Wesselink, A. J., Paranya, K., & de Vorkin, K. 1972, A&AS, 7, 257
Whitelock, P. A. 1987, PASP, 99, 573
Willson, L. A. 2000, ARA&A, 38, 573
Willson, L. A., & Kim, A. 2004, in ASP Conf. Ser. 313, Asymmetrical Planetary Nebulae III: Winds, Structure and the Thunderbird, ed. M. Meixner et al. (San Francisco: ASP), 394
Wilson, R. W., Baldwin, J. E., Buscher, D. F., & Warner, P. J. 1992, MNRAS, 257, 369
Wittkowski, M., Langer, N., & Weigelt, G. 1998, A&A, 340, L39
Wood, B. E., & Karovska, M. 2004, ApJ, 601, 502
Zuckerman, B., & Aller, L. H. 1986, ApJ, 301, 772